Supporting information

Laser-induced oxygen vacancies in $FeCo_2O_4$ nanoparticles for boosting oxygen evolution and reduction

1. Sample Preparation

Synthesis of $FeCo_2O_4$ microspheres: In a typical synthesis, 1 mmol of $FeCl_2 \cdot 4H_2O$ and 2 mmol of $Co(NO_3)_2 \cdot 6H_2O$ were dissolved into 40 mL of ethanol at room temperature with stirring 30 mins. Then, this transparent solution was transferred to a 50 mL autoclave, which was allowed to react at 180 °C for 20 h. The final black products were collected and washed with deionized water and absolute ethanol several times, followed by annealing at 400 °C for 2 h in air.

Synthesis of $FeCo_2O_4$ nanoparticles: $FeCo_2O_4$ nanoparticles rich in oxygen vacancies (R-$FeCo_2O_4$) were synthesized by laser fragmentation of $FeCo_2O_4$ microspheres at room temperature. The laser source is a nanosecond pulsed Nd:YAG laser (Nimma-600 from Beamtech) with wavelength of 532 nm, pulse width 7 ns, and power density 300 Wcm^{-2}. First, 5 mg as-prepared $FeCo_2O_4$ microspheres were dispersed in 20 ml deionized water, transferred the solution into a 50 ml flask with three necks, and then the suspension was stirred and irradiated by nanosecond laser for 30 min at room temperature, leading to the transformation into a brown colloid. Finally, the product was centrifuged at 15000 rpm for 30 min and dried for 12 h. For comparison, the $FeCo_2O_4$ nanoparticles poor in oxygen vacancies (P-$FeCo_2O_4$) was synthesized, introducing O_2 into deionized water to form O_2-saturated solution, and then use the same procedure with the O_2 flow (20 sccm) during the reaction. The $FeCo_2O_4$ nanoparticles were also fabricated with Ar and air flow into to solution for further comparion.

2. Characterization

The structure and crystal phase were determined XRD (Siemens-Bruker D5000). SEM was carried out by S4800 (Hitachi), TEM and high-resolution TEM was carried out by using JEOL 2100 Cryo microscope at an acceleration voltage of 200 Kv equipped with a field-emission gun and an Oxford INCA energy-dispersive X-ray

spectroscopy (EDS) module. XPS analyses were conducted on a k-alpha Thermo fisher spectrometer (ThermoFisher Scientific).

3. Electrochemical measurements

Electrocatalytic oxygen evolution reaction (OER) testing: Electrochemical measurements were performed with a three-electrode cell configuration. A platinum sheet was used as the counter electrode while Ag/AgCl electrode was used as the reference. 5 mg of catalysts, 5 mg of carbon powders (Vulcan XC 72) and 50 µl of 5 wt% Nafion solution were dispersed in 1 ml water by 30 min sonication to form a homogeneous ink. Then the catalyst ink was dropped onto a carbon fiber and slowly dried to make a thin film working electrode with a catalysts loading mass of about 0.2 mg cm^{-2}. The reference electrode was calibrated in O_2-saturated 0.1 M KOH.

To measure double-layer charging via CV, a potential range in which no apparent Faradaic processes occur was determined from static CV. This range is typically a 0.1 V potential window centered at the open-circuit potential (OCP) of the system. All measured current in this non-Faradaic potential region is assumed to be due to double-layer charging. The charging current, i_c, is then measured from CVs at multiple scan rates. The working electrode was held at each potential vertex for 10 s before beginning the next sweep. The double-layer charging current is equal to the product of the scan rate, v, and the electrochemical double-layer capacitance, C_{DL}, was given as below:

$$i_c = vC_{DL}$$

The ECSA of a catalyst sample is calculated from the double-layer capacitance as below:

$$ECSA = C_{DL}/C_S$$

where C_s is the specific capacitance of the sample or the capacitance of an atomically smooth planar surface of the material per unit area under identical electrolyte conditions, we use general specific capacitances of $C_s = 0.04$ mF cm^{-2} in 0.1M KOH, the geometric area of the electrode, 0.071 cm^2.

Electrocatalytic oxygen reduction reaction (ORR) testing: The electrochemical

properties of the as-prepared samples were investigated with the same instrument. A flow of O_2 was maintained over the electrolyte (0.1 M KOH) during the recording of electrochemical measurements in order to ensure the O_2/H_2O equilibrium at 1.23 V vs. RHE. Cyclic voltammetry was performed from 1.05 to 0.35 V vs. RHE at 5 mV s^{-1} after purging the electrolyte with O_2 gas for 30 min. Polarization curves were obtained in an O_2 saturated 0.1 M KOH solution with a scan rate of 5 mV s^{-1} and a rotation rate of 1600 rpm. Tafel slopes were derived from polarization curves. The electron transfer number (n) was calculated by Koutecky-Levich plots.

$$1/i = 1/B\omega^{1/2} + 1/i_K$$

$$B = 0.2nFAC_0D^{2/3}\vartheta^{-1/6}$$

where i_K is the kinetic current in amperes at a constant potential, i is the measured current on RDE, ω is the electrode rotating speed in rpm, B is the reciprocal of the slope, n is the number of electrons transferred per oxygen molecule, A is the area of electrode, F is the Faraday constant, D is the diffusion coefficient of O_2 in 0.1 M KOH, υ is the kinetic viscosity of electrolyte, and C_0 is the bulk concentration of O_2. The constant 0.2 is adopted when the rotating speed is expressed in rpm.

Znic-air batteries (ZABs) testing: Primary Zn-air batteries were performed on home-built electrochemical cells. A polished Zn plate was used as the anode, R-FeCo$_2$O$_4$, commercial Pt/C (20 wt%, Johnson Matthey) and RuO$_2$ catalyst ink were prepared by dispersing 5 mg catalyst in 1 mL deionized water and 40 μL Nafion solution. The R-FeCo$_2$O$_4$, Pt/C and RuO$_2$ catalyst ink were then coat on carbon fiber paper to achieve a mass loading of 0.5 mg cm^{-2}. All data were collected from the as-fabricated cell with a wave drive 20 workstation (Pine Research Instruments, US) at room temperature. The specific capacity (mAh g^{-1}) was calculated according to the following equation:

$$Specific\ capacity = I \times t / m_{Zn}$$

where I is the current, t is the service time in hour, V is the average discharge voltage, and m_{Zn} is the weight of consumed zinc electrode.
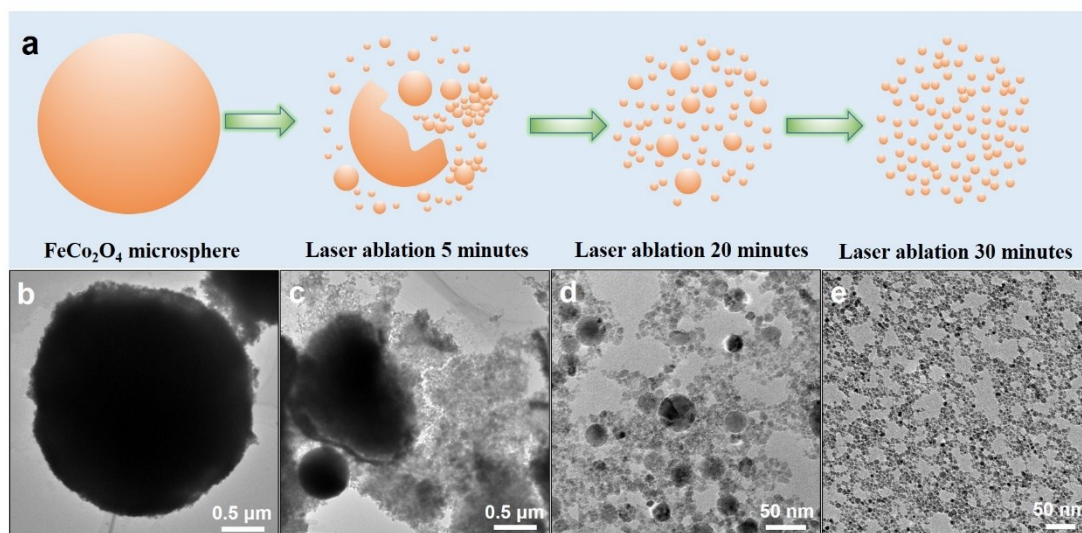
Fig. S1. (a) Schematic illustration of the fabrication processes of R-FeCo$_2$O$_4$; (b-d) The corresponding TEM images of FeCo$_2$O$_4$ at different reaction time.
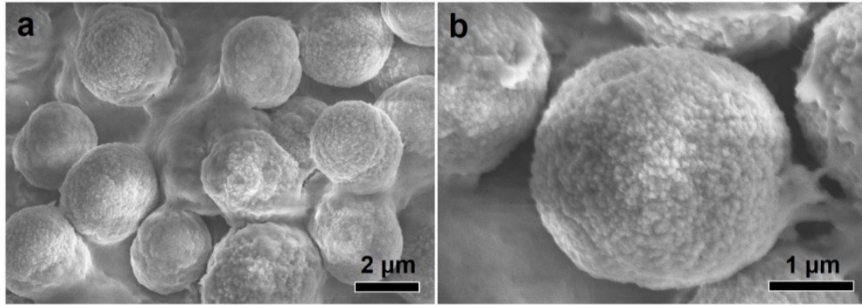
Fig. S2. SEM images of FeCo$_2$O$_4$ microspheres.
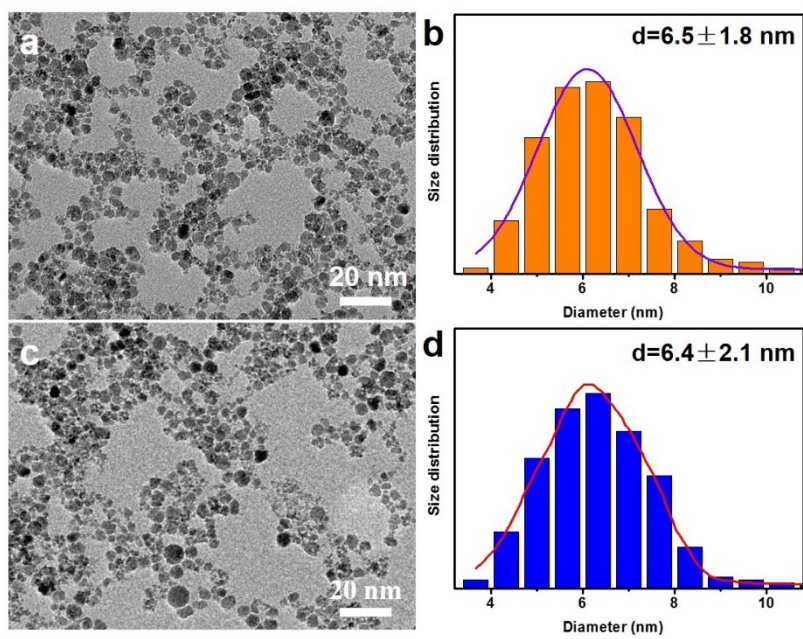
Fig. S3. (a) TEM image and (b) size distribution of R-FeCo$_2$O$_4$; (c) TEM image and (d) size distribution of P-FeCo$_2$O$_4$.
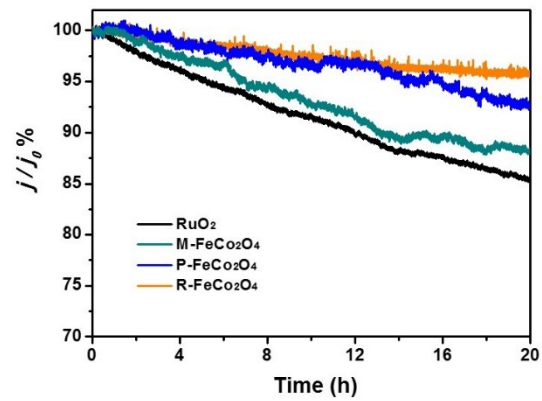
Fig. S4. Chronoamperometry testing for R-FeCo$_2$O$_4$, P-FeCo$_2$O$_4$, M-FeCo$_2$O$_4$ and RuO$_2$ at 1.6 V.
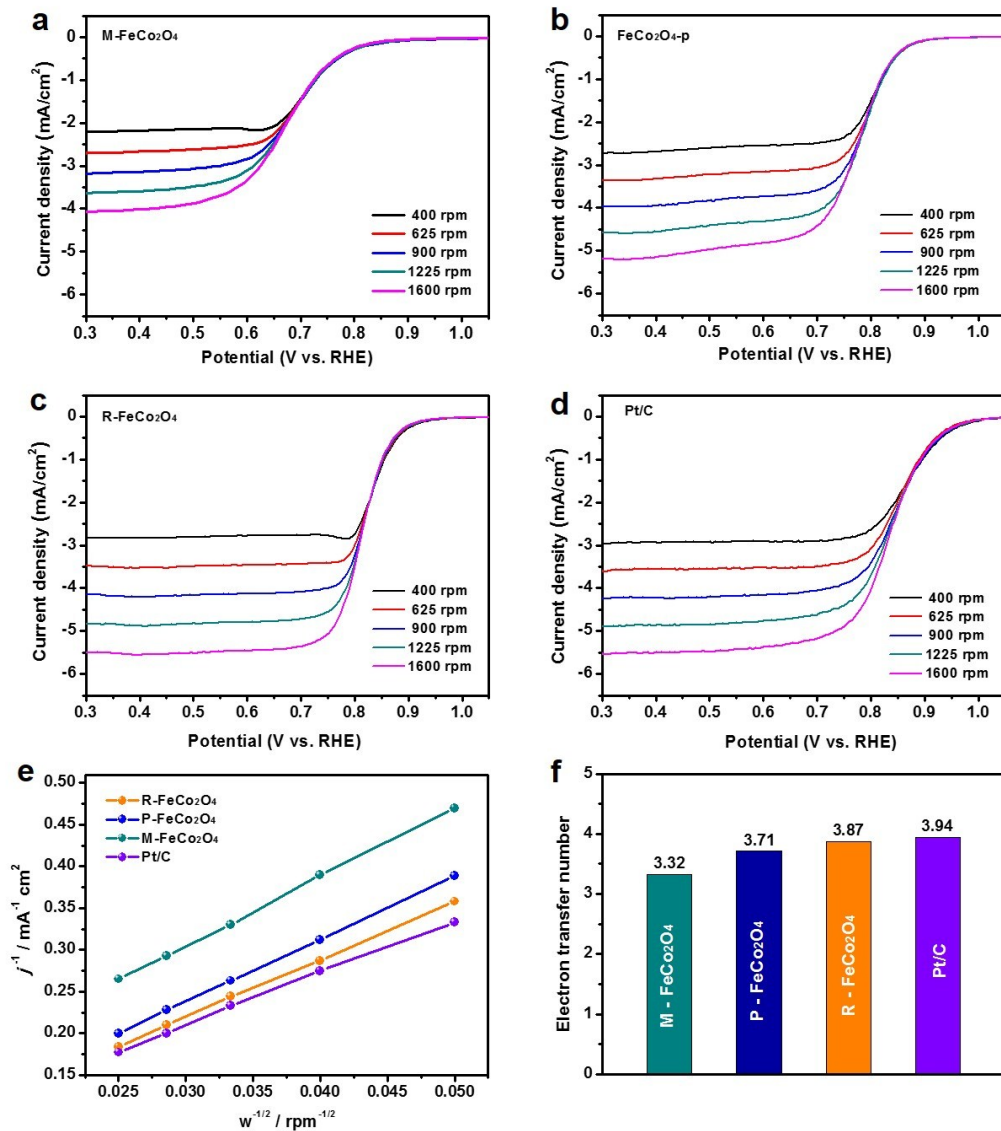
Fig. S5. LSVs with different scanning rates for (a) M-FeCo$_2$O$_4$, (b) P-FeCo$_2$O$_4$, (c) R-FeCo$_2$O$_4$ and (d) Pt/C; (e) the corresponding Koutecky-Levich (K-L) plots for different catalysts; (f) calculated electron-transfer number from K-L plots.
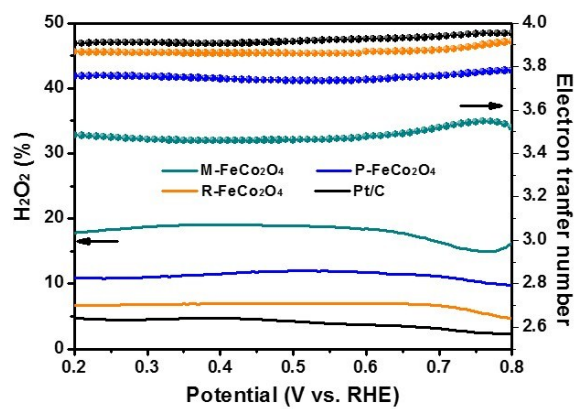
Fig. S6. Calculated electron-transfer number and H_2O_2 yield of R-FeCo$_2$O$_4$-r, P-FeCo$_2$O$_4$-p, M-FeCo$_2$O$_4$ and Pt/C from rotating ring-disk electrode date.
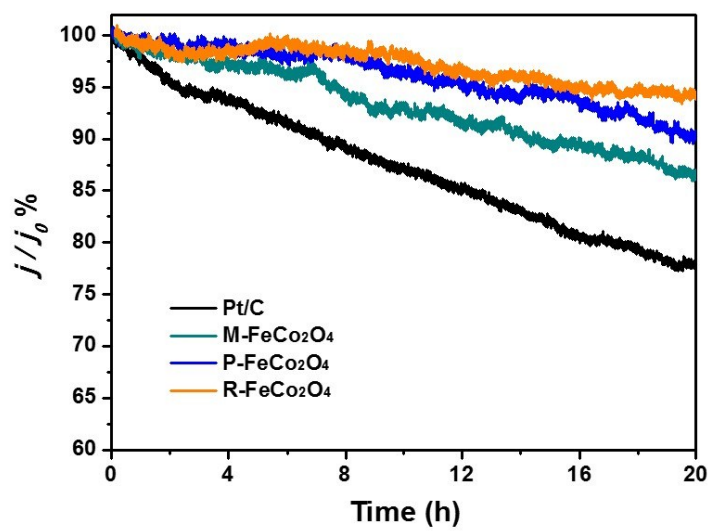
Fig S7. Chronoamperometry testing for R-FeCo$_2$O$_4$-r, P-FeCo$_2$O$_4$-p, M-FeCo$_2$O$_4$ and Pt/C at 0.5 V.
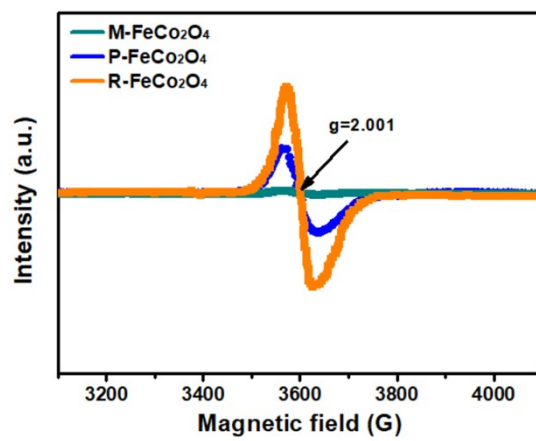
Fig. S8 EPR spectra of M-FeCo$_2$O$_4$, P-FeCo$_2$O$_4$ and R-FeCo$_2$O$_4$.
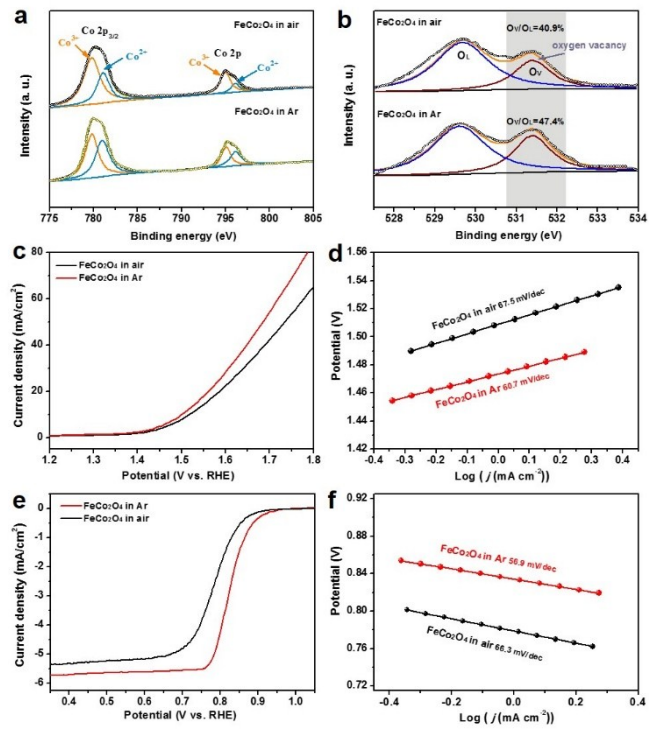
Fig. S9. Characterizations on oxygen vacancies and their catalytic activities $FeCo_2O_4$ in air and $FeCo_2O_4$ in Ar. (a) Fitted Co 2p spectra for $FeCo_2O_4$ in air and $FeCo_2O_4$ in Ar; (b) Fitted O 1s spectra for $FeCo_2O_4$ in air and $FeCo_2O_4$ in Ar; (c-f) The OER/ORR performance of $FeCo_2O_4$ in air and $FeCo_2O_4$ in Ar.
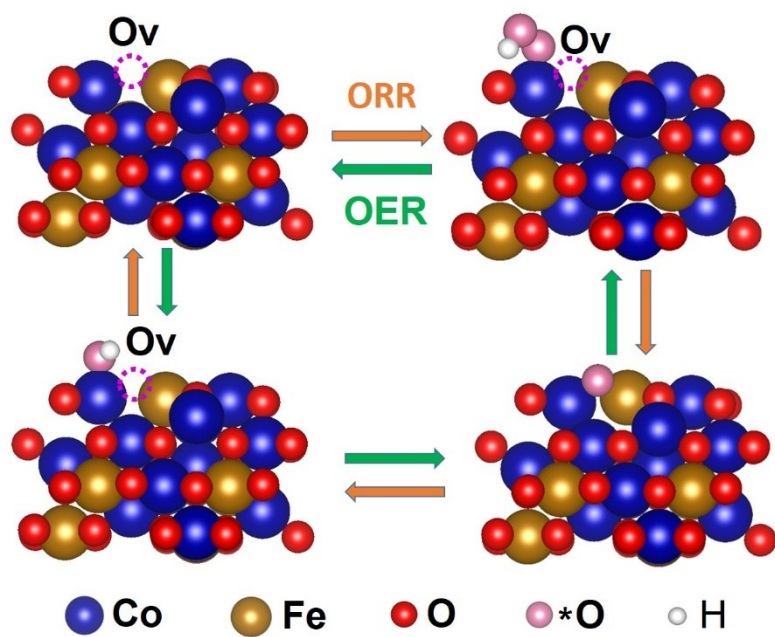
Fig. S10 DFT model of FeCo$_2$O$_4$ with oxygen vacancies for ORR/OER.
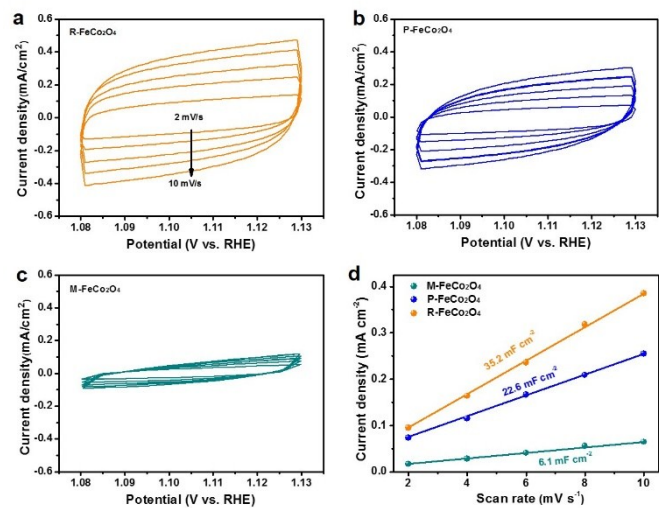
Fig. S11 Cyclic voltammograms of (a) R-FeCo$_2$O$_4$, (b) P-FeCo$_2$O$_4$, (c) M-FeCo$_2$O$_4$ measured at scan rates from 2 to 10 mV /s; (d) the corresponding charging current density plots with different scan rates for catalysts.
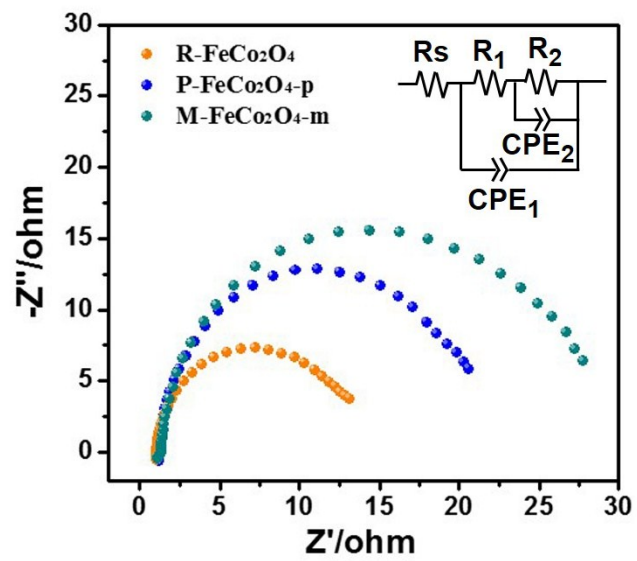
Fig. S12. EIS spectra and equivalent circuit (inset) of different catalysts recorded at 1.6 V.
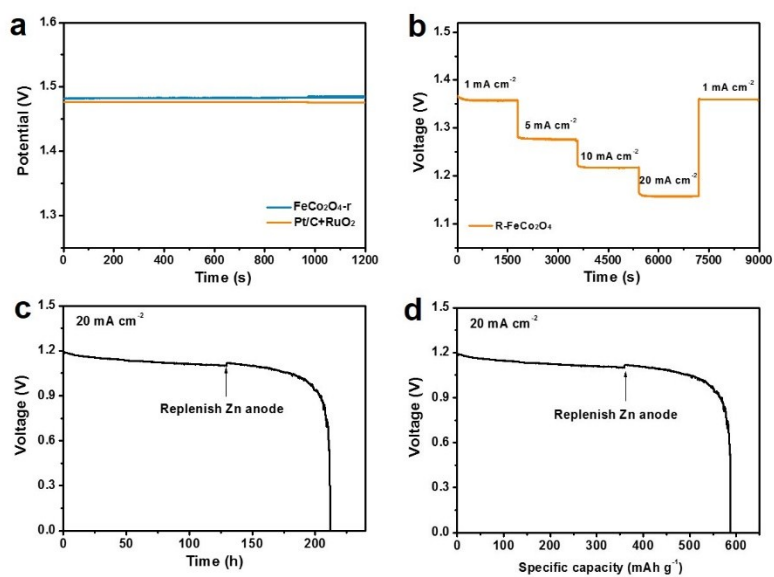
Fig. S13. (a) Open-circuit plots of zinc-air batteries with R-FeCo$_2$O$_4$ as cathodes in 6 M KOH aqueous solution, (b) rate discharge curves of zinc-air battery with R-FeCo$_2$O$_4$ as cothode at different current densities, (c, d) the typical deep discharge curve and specific capacity of the zinc-air battery at 20 mA cm^{-2}.

Table S1. Comparison of OER performance of R-FeCo$_2$O$_4$ with reported metal oxides catalysts.

Catalysts	Overpotential (mV) @ 10 mA cm^{-2}	Tafel slopes (mV cm^{-2})	References
R-FeCo$_2$O$_4$	276	61	This work
P-FeCo$_2$O$_4$	297	72	This work
M-FeCo$_2$O$_4$	363	115	This work
NCNT/Co$_{0.51}$Mn$_{0.49}$O	340	40	1
MnCo$_2$O$_4$/N-rmGO	350		2
Ni$_{0.75}$Co$_{0.25}$O$_x$	336	33	3
Co$_3$O$_4$/N-rmGO	312	67	4
N-CG-CoO	340	71	5
Zn$_x$Co$_{3-x}$O$_4$	320	51	6
Ni$_x$Co$_{3-x}$O$_4$	370	59-64	7
ZnCo$_2$O$_4$/N-CNT	420	70	8
ZnCo$_2$O$_4$	460	90	8

Table S2. Comparison of ORR performance of R-FeCo$_2$O$_4$ with reported metal oxides catalysts at 1600 rpm on glass carbon electrode.

Catalysts	$E_{1/2}$ (V)	Onset potentials (V)	Tafel slopes (mV Dec^{-1})	References
R-FeCo$_2$O$_4$	0.82	0.95	57	This Work
P-FeCo$_2$O$_4$	0.77	0.9	70	This Work
M-FeCo$_2$O$_4$	0.68	0.86	110	This Work
NCNT/Co$_{0.51}$Mn$_{0.49}$O	0.84	0.96	54	1
ZnCo$_2$O$_4$/N-CNT	0.87	0.95	53	8
ZnCo$_2$O$_4$	0.84	0.87	81	8
Mn-Co oxides	0.77	0.86	42	9
Co$_{0.50}$Mo$_{0.50}$O$_y$N$_z$/C	0.76	0.92	71	10
N-CG-CoO	0.81	0.90	48	11
Co$_3$O$_4$/N-rmGO	0.83		42	4
CoO/N-CNT	0.86	0.93		12

References

1. X. Liu, M. Park, M. G. Kim, S. Gupta, X. J. Wang, G. Wu and J. Cho, *Nano Energy*, 2016, **20**, 315-325.

2. Y. Y. Liang, H. L. Wang, J. G. Zhou, Y. G. Li, J. Wang, T. Regier and H. J. Dai, *Journal of the American Chemical Society*, 2012, **134**, 3517-3523.

3. L. Trotochaud, J. K. Ranney, K. N. Williams and S. W. Boettcher, *Journal of the American Chemical Society*, 2012, **134**, 17253-17261.

4. Y. Y. Liang, Y. G. Li, H. L. Wang, J. G. Zhou, J. Wang, T. Regier and H. J. Dai, *Nature Materials*, 2011, **10**, 780-786.

5. S. Mao, Z. H. Wen, T. Z. Huang, Y. Hou and J. H. Chen, *Energy & Environmental Science*, 2014, **7**, 609-616.

6. X. J. Liu, Z. Chang, L. Luo, T. H. Xu, X. D. Lei, J. F. Liu and X. M. Sun, *Chemistry of Materials*, 2014, **26**, 1889-1895.

7. Y. G. Li, P. Hasin and Y. Y. Wu, *Advanced Materials*, 2010, **22**, 1926-1929.

8. Z. Q. Liu, H. Cheng, N. Li, T. Y. Ma and Y. Z. Su, *Advanced Materials*, 2016, **28**, 3777-3784.

9. L. L. Yao, W. X. Yang, H. L. Liu, J. B. Jia, G. H. Wu, D. Liu, T. Liu, T. X. Tan and C. Wang, *Dalton Transactions*, 2017, **46**, 15512-15519.

10. B. F. Cao, G. M. Veith, R. E. Diaz, J. Liu, E. A. Stach, R. R. Adzic and P. G. Khalifah, *Angewandte Chemie International Edition*, 2013, **52**, 10753-10757.

11. S. Mao, Z. H. Wen, T. Z. Huang, Y. Hou and J. H. Chen, *Energy & Environmental Science*, 2014, 7, 609-616.

12. Y. Y. Liang, H. L. Wang, P. Diao, W. Chang, G. S. Hong, Y. G. Li, M. Gong, L. M. Xie, J. G. Zhou, J. Wang, T. Z. Regier, F. Wei and H. J. Dai, *Journal of the American Chemical Society*, 2012, **134**, 15849-15857.

13. L. Z. Zhuang, Y. Jia, T. W. He, A. J. Du, X. C. Yan, L. Ge, Z. H. Zhu and X. D. Yao, *Nano Research*, 2018, **11**, 3509-3518.

14. L. Xu, Q. Q. Jiang, Z. H. Xiao, X. Y. Li, J. Huo, S. Y. Wang and L. M. Dai, *Angewandte Chemie International Edition*, 2016, **55**, 5277-5281.